Stellar neutron capture cross sections of the Gd isotopes

K. Wisshak, F. Voss, and F. Käppeler
Forschungszentrum Karlsruhe, Institut für Kernphysik, Postfach 3640, D-76021 Karlsruhe, Germany

K. Guber
Oak Ridge National Laboratory, Oak Ridge, Tennessee 37831

L. Kazakov and N. Kornilov
Institute for Physics and Power Engineering, Obninsk-Kaluga Region, Russia

M. Uhl*
Institut für Radiumforschung und Kernphysik, Boltzmanngasse 3, A-1090 Wien, Austria

G. Reffo
ENEA, Centro Dati Nucleari, Via Martiri di Monte Sole 4, I-40138 Bologna, Italy
(Received 11 May 1995)

The neutron capture cross sections of ^{152}Gd, ^{154}Gd, ^{155}Gd, ^{156}Gd, ^{157}Gd, and ^{158}Gd were measured in the energy range from 3 to 225 keV at the Karlsruhe 3.75 MV Van de Graaff accelerator. Neutrons were produced via the ^{7}Li$(p,n)^{7}$Be reaction by bombarding metallic Li targets with a pulsed proton beam. Capture events were registered with the Karlsruhe 4π Barium Fluoride Detector, which was improved by replacing crystals with high α background and by introducing a pierced crystal at zero degrees with respect to the beam axis. These changes resulted in a significantly increased efficiency for capture events. The main experimental problem was that the samples of the two s isotopes ^{152}Gd and ^{154}Gd showed only relatively low enrichment. Nevertheless, the spectroscopic quality of the BaF_2 detector allowed evaluation of the corresponding corrections for isotopic impurities reliably. The cross section ratios could be determined with an overall uncertainty of typically 1%, an improvement by factors of five to ten compared to existing data. Severe discrepancies were found with respect to previous results. Maxwellian averaged neutron capture cross sections were calculated for thermal energies between $kT=10$ keV and 100 keV. The new stellar cross sections were used for an updated analysis of the s-process reaction flow in the mass region between samarium and gadolinium, which is characterized by branchings at ^{151}Sm, ^{154}Eu, and ^{155}Eu. With the classical approach, the s-process temperature could be constrained corresponding to a range of thermal energies between $kT=28$ and 33 keV. The ^{152}Gd production in low mass stars was found to depend strongly on the neutron freeze-out at the end of the helium shell burning episodes.

PACS number(s): 25.40.Lw, 27.70.+q, 97.10.Cv, 98.80.Ft

I. INTRODUCTION

The present experiment on the gadolinium isotopes continues the accurate determination of neutron capture cross sections for s-only isotopes with the Karlsruhe 4π BaF_2 detector. After tellurium [1], samarium [2], and barium [3], gadolinium is the fourth of the six elements with two even s-only isotopes. As described in the above references these cases are important for investigating the related s-process branchings in great detail, in particular with respect to the physical conditions in the helium burning zones of Red Giant stars.

The neutron capture path from samarium to gadolinium (Fig. 1) shows that the two isotopes ^{152}Gd and ^{154}Gd are shielded from the r process by their stable samarium isobars. The unstable isotopes ^{151}Sm, ^{154}Eu, and ^{155}Eu are possible branching points due to the competition between neutron captures and β decays. These β decays — and hence the related branchings — are affected by the stellar temperature because these nuclei, particularly ^{151}Sm, have low-lying excited levels with temperature dependent populations in stellar interiors. In addition, there is also a weak dependence on electron density for the decays of ^{151}Sm, ^{152}Eu, and ^{155}Eu. Accordingly, the resulting abundance pattern may yield information on the temperature and the electron density (and therefore the mass density) during the s process.

The branchings are characterized by the branching factor $f_n=\lambda_n/(\lambda_n+\lambda_\beta)$, where $\lambda_n = n_n v_T \langle\sigma\rangle$ denotes the neutron capture rate and $\lambda_\beta=\ln 2/t_{1/2}$ the β-decay rate. In these expresions $t_{1/2}$ is the half-life, n_n the s-process neutron density, $v_T = (2kT/\mu)^{1/2}$ the mean thermal velocity, and $\langle\sigma\rangle$ the Maxwellian averaged cross section. The quantity μ is the reduced mass. For the branchings at the tellurium, samarium, and barium isotopes [1–3], the branching factors, f_n, were small and of the order of 0.1. This implies that only a small part of the s-process flow is bypassing the lighter s-only isotope and that the $N_s\langle\sigma\rangle$ values of both s isotopes are about equal. The branching at ^{151}Sm shows an opposite behavior. Now, f_n is of the order of 0.90, and most of the

*Deceased.

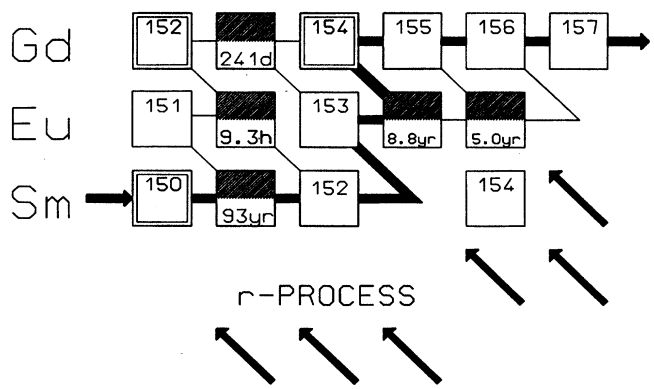

FIG. 1. The s-process path in the region of the gadolinium isotopes.

s-process flow is bypassing ^{152}Gd. Changing the cross section ratio of the s-only isotopes by 1% in the samarium and barium cases results in a 10% change of f_n, indicating that the sensitivity of the branching to f_n and, hence, to the neutron flux is large. Clearly, the uncertainty of the cross section measurement determines the uncertainty of the derived neutron flux. In case of ^{152}Gd, the situation is opposite: a 1% change in the cross section affects the branching factor only by 1%, resulting in a low sensitivity for the neutron flux. However, the sensitivity is shifted to the β-decay part of the branching, since now $f_\beta = 1-f_n$ is small. Therefore, this branching is suited for determining the s-process temperature via the temperature-dependent half-life of ^{151}Sm [4].

The branching at ^{154}Eu is of the first type with a small branching factor, f_n. Since both s-only isotopes, ^{152}Gd, and ^{154}Gd are partly bypassed (Fig. 1), the full reaction flow has to be normalized at ^{150}Sm, the closest s-only isotope that is not affected by branchings. This implies an additional uncertainty via the elemental abundance ratio of Sm and Gd. However, this ratio is known to $\pm 1.3\%$ [5], due to the chemical similarity of these rare earth elements.

The isotope ^{152}Gd was long considered to exhibit a strong p-process component [6] according to the systematics of neighboring p-only nuclei such as ^{156}Dy, ^{154}Dy, or ^{144}Sm. In contrast, recent model calculations indicate that the p-process yield of ^{152}Gd is much smaller, probably not exceeding 12% [7,8]. This means that $\approx$90% of the observed ^{152}Gd must be ascribed to neutron capture reactions in the s process. By far the largest part is certainly produced during helium shell burning in low mass stars of 1 to 3 solar masses. This site is responsible for the main s-process component, which accounts for practically all s abundances between zirconium and bismuth. However, it was found recently [9] that there is also a small but significant contribution to ^{152}Gd by the weak s-process component, which is associated with core helium burning in massive stars of more than 15 solar masses. This scenario contributes predominantly to the mass region $A \leq 90$, but is much less efficient in the region, where the main component dominates. Only a few rare isotopes, which are partly bypassed by the reaction flow of the main component, are noticeably produced in this scenario. The average over a generation of massive stars yields about 6% of the observed ^{152}Gd [9]. Accordingly, at least 80% have to be accounted for by low mass stars.

The ^{151}Sm branching is also interesting with respect to the pulsed s-process scenario suggested by stellar models [10,11]. The β decay of ^{151}Sm in the interpulse phase may increase the amount of ^{152}Gd compared to a steady flow situation. This aspect can be tested with improved cross sections as well.

The analysis of the s-process branchings defined by ^{152}Gd and ^{154}Gd is confronted with the additional problem that not only the β-decay rates of the branch point isotopes, but also the neutron capture rates may depend on temperature, in particular those of ^{152}Sm and ^{154}Gd [12,13]. Existing model calculations yield contradictory values for this effect, an uncertainty that can possibly be constrained by the s-process abundance systematics.

The experimental status of the gadolinium cross sections is unsatisfactory. The two s-only isotopes ^{152}Gd and ^{154}Gd have low natural abundances of 0.20 and 2.18%, respectively. Therefore, highly enriched samples are not available. In a previous experiment, the enrichments were 32% for ^{152}Gd and 66% for ^{154}Gd [6], leading to large corrections for isotopic impurities. These corrections are particularly difficult to deal with in experiments based on the pulse height weighting technique [6], where the efficiency for capture events is proportional to the binding energy. Therefore, it is larger for odd than for even isotopes. Since the magnitude of the cross sections is also correlated with the binding energy, this effect is further enhanced, resulting in an $\sim$80% correction for isotopic impurities in the most recent measurement on ^{152}Gd [6]. In view of the large discrepancies between calculated and measured weighting functions [14], the correlated systematic uncertainty is certainly a problem, which is aggravated by the fact that two of the major impurity isotopes, ^{156}Gd and ^{158}Gd, were not included in that experiment.

With the Karlsruhe $4\pi BaF_2$ detector this situation is quite different since the efficiency is equal for odd and even isotopes. In addition, the good resolution in γ-ray energy allows one to distinguish capture events from odd and even isotopes by their different binding energies, so that the contributions from odd impurities can be partly separated from the capture events of the even isotopes. The isotopic corrections could be determined from a nearly complete set of 6 isotopes which were investigated simultaneously. The only missing stable isotope was ^{160}Gd, but its influence was small because its cross section is lower by a factor of 7 compared to the s-only isotopes. Therefore, this correction could be determined with considerably improved reliability.

Apart from the problems with the isotopic corrections, the experimental situation is quite similar to that in the measurement of the samarium cross sections [2]. Since the ratio of total to capture cross sections is only between 10 and 30, backgrounds from scattered neutrons are small, thus yielding a favorable signal to background ratio.

Experiment and data analysis are described in Secs. II and III. The differential cross sections are presented in Sec. IV, and the uncertainties are discussed in Sec. V. The determination of stellar cross sections and the discussion of the astrophysical implications are presented in Secs. VI and VII. A detailed description of the present experiment, including data

TABLE I. Sample characteristics.

Sample[a]	Thickness (mm)	Thickness (10^{-3} at/b)[e]	Weight[b] (g)	Can[c] (g)	Impurity[d] (%)[f]	Neutron binding energy (MeV)
^{158}Gd	5.8	8.6244	4.6062	0.3459	<0.3	5.943
Graphite	2.5	21.6874	0.7644	0.2136		
^{152}Gd	1.6	2.1742	1.1427	0.1890	<0.1	6.247
^{197}Au	0.3	2.2475	1.2990	0.1849		6.513
^{154}Gd	1.8	2.4185	1.2677	0.1830	<0.4	6.439
^{155}Gd	0.9	1.3086	0.6878	0.1830	<0.1	8.536
^{156}Gd	2.3	3.1241	1.6507	0.2138	<0.2	6.360
^{157}Gd	1.7	2.3882	1.2689	0.1805	<0.2	7.937
Empty	0.3			0.1810		

[a]All samples 15 mm in diameter.
[b]For gadolinium samples: weight of Gd_2O_3.
[c]Aluminum box.
[d]Elements apart from oxygen.
[e]For gadolinium samples: sum of all Gd isotopes.
[f]% of weight.

evaluation methods, calculation of correction factors, and presentation of the results from individual runs can be found in Ref. [15].

II. EXPERIMENT

A. Experimental method

The neutron capture cross sections of the gadolinium isotopes 152 and 154 to 158 have been measured in the energy range from 3 to 225 keV using gold as a standard. Since the experimental method has been published in detail [1,2,16,17], only a more general description is given here, complemented with the specific features of the present measurement. Neutrons were produced via the ^{7}Li$(p,n)^7$Be reaction by bombarding metallic Li targets with the pulsed proton beam of the Karlsruhe 3.75 MV Van de Graaff accelerator. The neutron energy was determined by time of flight (TOF), the samples being located at a flight path of 78.8 cm. The important parameters of the accelerator were pulse width <1 ns, repetition rate 250 kHz, and average beam current 1.5 μA. In different runs, the proton energies were adjusted 30 and 100 keV above the threshold of the ^{7}Li$(p,n)^7$Be reaction at 1.881 MeV. In all runs, the lithium targets were sufficiently thick to slow down the protons below the reaction threshold. In this way, continuous neutron spectra in the energy range of interest for s-process studies were obtained, ranging from 3 to 100 keV, and 3 to 200 keV, respectively. Below 3 keV, the signal to background ratio in the TOF spectra becomes too small for a meaningful analysis. The run with lower maximum energy offers a significantly better signal to background ratio.

Capture events were registered with the Karlsruhe 4π Barium Fluoride Detector via the prompt capture γ-ray cascades. This detector consists of 42 hexagonal and pentagonal crystals forming a spherical shell of BaF_2 with 10 cm inner radius and 15 cm thickness. It is characterized by a resolution in γ-ray energy of 7% at 2.5 MeV, a time resolution of 500 ps, and a peak efficiency of 90% at 1 MeV. For a comprehensive description see Ref. [16].

Previously, two of the 42 BaF_2 crystals had to be removed for the neutron beam to pass the detector, resulting in an effective solid angle of 94% of 4π. In the present experiment, a pierced crystal with a hole of 50 mm diameter was mounted at the exit of the neutron beam. The hole reduces the crystal volume only from 1.5 l to 1.2 l; thus the pierced crystal is increasing the total solid angle by 2%. The scintillation light is registered by a ring of 6 photomultiplier tubes (EMI9902 QKA) with 38 mm diameter.

Six crystals with high intrinsic backgrounds from a natural radium contamination ($\sim$1000 counts/s for the integral of the four α lines) have been replaced. Two of the new crystals have background rates of 200 counts/s as do most of the others, but four crystals exhibit very low radium impurities giving rise to less than 10 counts/s. With this change the total intrinsic background rate could be reduced by almost a factor of 2. This means that the threshold in the sum energy spectrum of the detector could be reduced from 2.4 to 1.4 MeV while recording the same integral count rate.

These two improvements, the increase in solid angle and the reduction of the sum energy threshold have led to a significantly increased detection efficiency (see Sec. III).

The experiment was divided into three runs, two with the conventional data acquisition technique in the calorimeter mode, and one with the analog-to-digital converter (ADC) system for obtaining more detailed spectroscopic information.

B. Samples

The samples have been prepared from isotopically enriched Gd_2O_3 powder. The relevant parameters of the samples are compiled in Table I. In addition to the six gadolinium samples, a gold sample, a graphite sample, and an empty position in the sample ladder were used in all runs. Compared to the previous experiment by Beer and Macklin [6], the sample masses could be reduced by factors of 2.3 to 8.6. Accordingly, the sample-related corrections for neutron multiple scattering and self-shielding were significantly smaller, and, therefore, less uncertain.

TABLE II. Isotopic compositions (%).

Sample	Isotope ^{152}Gd	^{154}Gd	^{155}Gd	^{156}Gd	^{157}Gd	^{158}Gd	^{160}Gd
^{152}Gd	32.50	5.45	16.68	15.56	9.03	12.13	8.65
^{154}Gd	0.0	57.00	32.70	5.30	2.10	1.90	1.00
^{155}Gd	<0.01	0.22	91.60	6.34	0.78	0.73	0.33
^{156}Gd	<0.1	0.20	1.30	93.50	3.30	1.30	0.40
^{157}Gd	<0.04	0.05	0.30	1.71	89.60	7.78	0.56
^{158}Gd	<0.08	<0.08	0.17	0.33	0.78	97.30	1.42

The samples were prepared in the same way as the samarium samples in Ref. [2]. When heated to 1000 °C, five of the samples lost less than 0.5% in weight, but for ^{156}Gd the loss was 10.7%. This shows strikingly that the contamination with water is a severe problem for the oxides of rare earth elements and has always to be checked. After heating, the composition of the samples was very stable and no further absorption of water was observed. In fact, the weight of all samples could be perfectly reproduced at the end of the measurements.

The isotopic composition of the samples is listed in Table II. Similar to the previous measurement [6] the enrichment of the ^{152}Gd and ^{154}Gd samples are rather low, 32.5% and 57.0%, respectively.

Despite their chemical stability the samples were canned in aluminum containers with 0.14 mm thick walls to avoid any losses of material. Accordingly, a bare aluminum can was mounted in the "empty" position of the sample ladder (Table I).

The neutron transmissions of the samples were calculated with the SESH code [18], and are generally larger than 95% . Since reliable total cross sections of the gadolinium isotopes were not available in the literature, the spectra measured with a ^{6}Li-glass detector at 260 cm flight path were used for a rough determination of the total cross sections. Though the accuracy of this method is inferior to that obtained in a dedicated experiment, the derived total cross sections are sufficient for the reliable calculation of the multiple scattering corrections (Sec. III). Normalization of the spectra to equal neutron flux was performed for all samples by means of a second ^{6}Li-glass monitor located close to the neutron target.

C. Measurements

The samples were moved cyclically into the measuring position by a computer controlled sample changer. The data acquisition time per sample was about 10 min, a complete cycle lasting about 1.5 h. From each event, a 64 bit word was recorded on magnetic tape containing the sum energy and TOF information together with 42 bits identifying those detector modules that contributed. Three runs were performed using neutron spectra with different maximum energies. The data in Run 3 were recorded with the ADC system. During the 44 days of data collection, the overall recorded information was 19 Gbyte.

III. DATA ANALYSIS

A. Total cross sections

The total cross sections of the gadolinium isotopes were determined in the neutron energy range from 10 to 200 keV via the TOF spectra measured with the ^{6}Li glass detector at a flight path of 260 cm. The total cross sections and the related uncertainties were obtained as described in Ref. [2], and are listed in Table III. The oxygen cross section was taken from a recent evaluation [Joint Evaluated File (JEF)] [19]. The total cross sections deduced for the carbon sample agree with the JEF data within $\pm 3.7\%$, comparable to the results reported in Ref. [2], where systematic differences of 3% were found. This difference may be due to the fact that the sample diameter of 15 mm is just sufficient to shade the lithium glass scintillator. Hence even a small misalignment of the detector could have caused the observed deviations. Correspondingly, this effect was avoided in the barium experiment [3], where the larger sample diameter of 22 mm resulted in a significantly better agreement with the evaluated total cross section of carbon.

In view of this difficulty only rough estimates for the total cross sections of the gadolinium isotopes were obtained. For the isotopes ^{152}Gd and ^{154}Gd, additional uncertainties due to the sizable isotopic corrections had to be considered. The total cross section of elemental gadolinium calculated from the isotopic cross sections of Table III and assuming the cross sections for ^{158}Gd and ^{160}Gd to be equal, is about 10% larger than the data given in Ref. [20].

TABLE III. The measured total cross sections (determined from the count rate of the ^{6}Li glass neutron monitor at 260 cm flight path).

Neutron energy (keV)	Total cross section (b) ^{152}Gd	^{154}Gd	^{155}Gd	^{156}Gd	^{157}Gd	^{158}Gd	^{12}C	^{197}Au
10–15	15.5	18.4	13.3	15.4	15.1	10.3	4.92	16.5
15–20	20.3	14.5	13.5	13.6	15.5	12.4	4.56	16.5
20–30	18.2	14.3	8.8	11.7	11.1	10.3	4.26	11.3
30–40	15.5	12.7	11.8	11.6	12.3	10.4	4.26	11.9
40–60	13.6	11.4	12.0	10.8	11.3	9.7	4.37	12.4
60–80	13.7	12.0	12.3	12.2	10.3	9.8	4.43	12.1
80–100	13.0	10.7	8.3	10.1	8.8	9.2	4.11	10.0
100–150	13.9	12.1	11.0	10.5	10.1	9.1	4.21	11.7
150–200	9.6	11.2	10.4	9.5	9.2	9.1	4.13	10.3
Uncertainty	~20%	~15%	24.9%	9.5%	12.4%	4.8%	3.7%	11.1%

TABLE IV. Matrix for isotopic correction (%) (using the approximation that the abundance of $^{160}Gd = 0.65 \times {}^{158}Gd$).

Corrected spectrum	Measured spectrum ^{152}Gd	^{154}Gd	^{155}Gd	^{156}Gd	^{157}Gd	^{158}Gd	Corrected sample thickness (10^{-3} at/b)
^{152}Gd	100	−8.4915	−24.2017	−10.3656	−8.2259	−4.2108	0.7066
^{154}Gd		100	−65.8754	−2.4846	−1.9211	−0.5735	1.3765
^{155}Gd		−0.1958	100	−2.8257	−0.3324	−0.1206	1.1959
^{156}Gd		−0.4427	−3.0621	100	−4.7786	−0.4579	2.9159
^{157}Gd		−0.0795	−0.4713	−1.3589	100	−2.2868	2.1368
^{158}Gd		+0.0092	−1.1804	−0.8933	−3.0953	100	8.4645

B. Capture cross sections

The data analysis was carried out analoguously to the procedure described previously [1,2,17]. All events were stored on tape and were sorted off-line into two-dimensional spectra containing 128 sum energy versus 2048 TOF channels according to various event multiplicities (Evaluation 1). In Evaluation 2, this procedure was repeated by rejecting those events, where only neighboring detector modules contributed to the sum energy signal. In this way, background from the natural radioactivity of the BaF_2 crystals and from scattered neutrons can be reduced. For all samples, the resulting spectra were normalized to equal neutron flux using the count rate of the second lithium glass monitor close to the neutron target. In all runs, the corresponding corrections were smaller than 0.3%. The calculation of the two-dimensional spectra from the data recorded with the ADC system is slightly more complicated and was performed as described in Ref. [2].

In the next step of data analysis, the spectra measured with the empty sample can were subtracted to remove sample-independent backgrounds. A remaining constant background was determined at very long flight times, where no time-correlated events are expected.

At this point, the spectra contain only events that are correlated with the sample. The next correction to be made is for isotopic impurities (see Ref. [2] for details). The respective coefficients are compiled in Table IV. To correct for ^{160}Gd impurities, the spectra of the ^{158}Gd sample were used, since this isotope has a very similar binding energy. The respective ^{160}Gd abundances, however, were scaled by a factor of 0.65 to account for its smaller capture cross section [21].

As noted before, the correction for isotopic impurities needs special consideration in the present experiment, particularly for the ^{152}Gd and ^{154}Gd samples. The left part of Fig. 2 shows the sum energy of the capture events in the ^{152}Gd sample before this correction. The spectrum exhibits clearly two peaks according to capture events in the even and odd isotopes, respectively. The right part of Fig. 2 shows the same spectrum after the correction. Comparison with the line shape of the ^{156}Gd sample, where the correction for isotopic impurities is small, indicates perfect agreement (see Fig. 5 and Ref. [15]).

Another important feature can be seen from Fig. 2 as well. Thanks to the good energy resolution of the detector, most of the capture events in the odd isotopes appear in the sum energy spectrum above the binding energies of the even isotopes. Since this energy range (above channel ~80) is not used for evaluating the cross sections of the even isotopes, these events can be completely suppressed. This distinction is a further advantage compared to experiments using detectors with poor energy resolution, where such a separation is impossible.

The magnitude of this correction is indicated in Fig. 3, showing the TOF spectra before background subtraction together with the background from isotopic impurities. The figure gives the worst case of the ^{152}Gd sample, where the correction accounts for about 50% of the observed effect. For the ^{154}Gd sample the respective value is 40% and for all other samples $\leq 5\%$ (for details see Ref. [15]). In a comparable experiment using the pulse height weighting technique, the observed effect of each isotope is proportional to $N\sigma B_n$, N being the abundance and B_n the binding energy. In this case, the respective correction for the ^{152}Gd sample can be estimated to 75%. This means that the correction for iso-

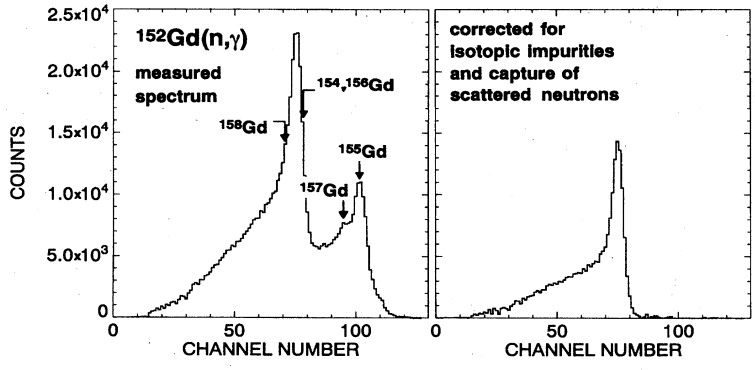

FIG. 2. Sum energy spectrum of the ^{152}Gd sample before and after correction for isotopic impurities and capture of scattered neutrons.

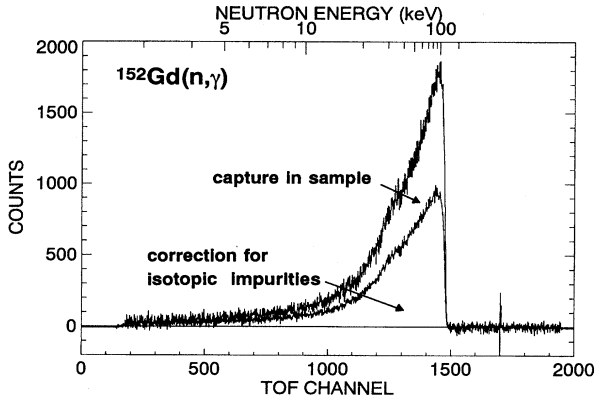

FIG. 3. TOF spectrum of the ^{152}Gd sample. The background due to isotopic impurities is shown separately.

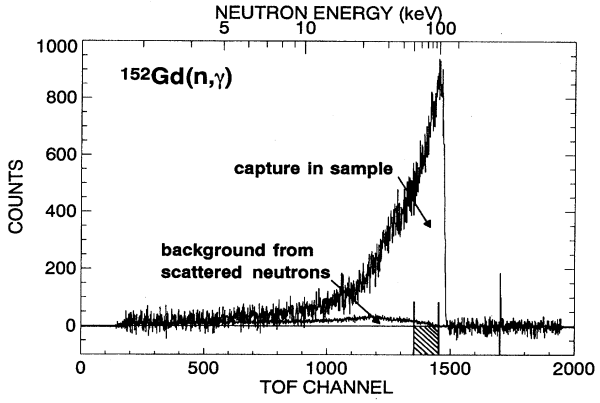

FIG. 4. TOF spectrum measured with the ^{152}Gd sample in run 3 with 100 keV maximum neutron energy. The background due to sample scattered neutrons is shown separately. The region used for the absolute normalization of the cross section is shown by a hatched box.

topic impurities exceeds the net effect of captures in ^{152}Gd by a factor 3.

Following the correction for isotopic impurities, the background due to capture of sample scattered neutrons was removed from the spectra by means of the data measured with the carbon sample. This correction is comparably small due to the favorable ratios of total and capture cross sections in the Gd isotopes, and was performed in the same way as described for the samarium isotopes [2]. After this last correction, the spectra contain only the net capture events of the respective isotopes.

The correction for capture of scattered neutrons is illustrated for the ^{152}Gd sample in Fig. 4. The worst case in this respect is ^{158}Gd, where this correction is two times larger. More details concerning the signal to background ratio are given in Ref. [15].

After background subtraction, the TOF spectra in Fig. 4 were used to determine the energy dependence of the cross section. For absolute normalization, the two-dimensional data were projected onto the sum energy using the TOF region of optimum signal to background ratio as indicated in Fig. 4 by a dashed box. The resulting pulse height spectra are shown in Fig. 5 for the events with multiplicity >2. Note that the threshold in sum energy could be lowered to 1.4 MeV.

In Fig. 6, the sum energy spectra are plotted for different multiplicities for the example of an odd and an even isotope. These multiplicities correspond to the number of detector modules contributing per event, while the true multiplicities are slightly smaller, because of cross talking between detector modules. In the even isotopes, 30 to 40% of the capture events are observed with multiplicities ≥ 5, the respective numbers being 50 to 60% for the odd isotopes. The arrows in Fig. 6 indicate the range of sum energy channels that were combined to yield the TOF spectra of Fig. 4, which were used to determine the cross section shapes.

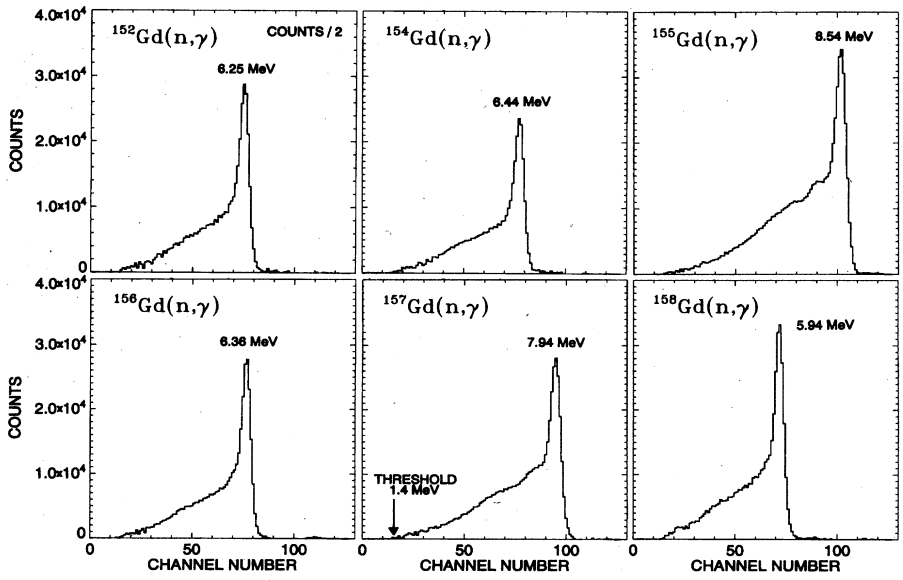

FIG. 5. Sum energy spectra of all isotopes measured in run 2 (200 keV maximum neutron energy) containing all events with multiplicity >2. These spectra were obtained by projection of the two-dimensional spectra in the TOF region below the maximum neutron energy as indicated by a hached box in Fig. 4

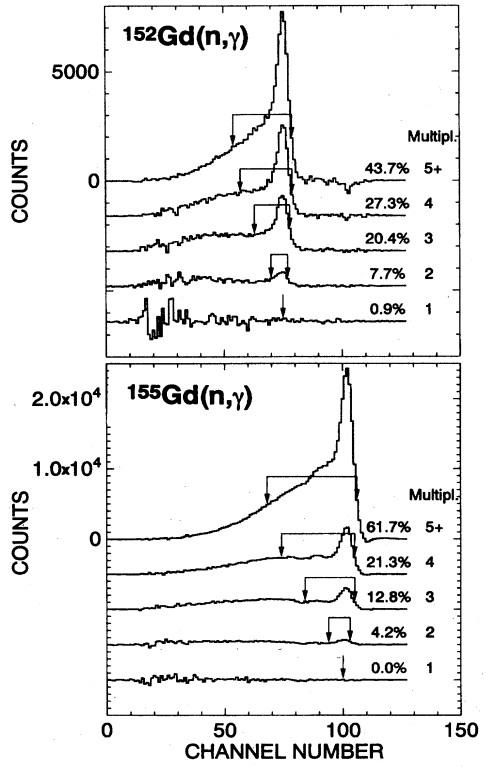

FIG. 6. Sum energy spectra of ^{152}Gd and ^{155}Gd and their dependencies on detector multiplicity. The regions used to determine the cross section shape are indicated by arrows.

The cross section ratio of isotope X relative to the gold standard is then

$$\frac{\sigma_i(X)}{\sigma_i(\mathrm{Au})} = \frac{\mathrm{Z_i(X)}}{\mathrm{Z_i(Au)}} \frac{\Sigma Z(\mathrm{Au})}{\Sigma Z(X)} \frac{\Sigma E(X)}{\Sigma E(\mathrm{Au})} \frac{m(\mathrm{Au})}{m(X)} F_1 F_2 . \quad (1)$$

In this expression, Z_i is the count rate in channel i of the TOF spectrum, ΣZ is the TOF rate integrated over the interval used for normalization (Fig. 4), ΣE is the total count rate in the sum energy spectrum for all multiplicities summed over the normalization interval (Fig. 5), and m is the sample thickness in atoms/barn. The factor $F_1 = [100\text{-}f(\mathrm{Au})]/[100\text{-}f(X)]$ corrects for the fraction of capture events f below the experimental threshold in sum energy, where X refers to the respective gadolinium sample (Table V), and F_2 is the respective ratio of the multiple scattering and self-shielding corrections.

The fraction of unobserved capture events, f, and the correction factor F_1 were calculated as described in detail in Ref. [17]. These calculations require the most representative neutron capture cascades and their relative contributions to the total capture cross section as well as the detector efficiency for monoenergetic γ rays in the energy range up to 10 MeV. Since this correction is limiting the accuracy of the experimental technique, these corrections were determined with two independent sets of capture cascades and capture γ-ray spectra of the involved isotopes, one calculated by Reffo according to the statistical and optical models [22] as in the previous measurements with the 4π BaF_2 detector [1–3], and a second set calculated by Uhl [23]. Both calculations are based on the Hauser Feshbach approach, but the way the gamma cascades are calculated is different (for details see Ref. [15]).

TABLE V. Fraction of undetected capture events, f (%), and the related correction factors (solid angle 96%, gamma-ray threshold 50 keV), F_1.

	Threshold in sum energy (MeV)				Assumption for gamma-ray cascades
	1.0	1.4	1.5	2.0	
f(Au)	2.16		3.30	4.93	Reffo
$f(^{152}$Gd)	1.08		2.07	3.42	
$f(^{154}$Gd)	0.82		1.62	2.80	
$f(^{155}$Gd)	0.45		0.89	1.23	
$f(^{156}$Gd)	0.96		1.49	2.98	
$f(^{157}$Gd)	0.55		1.13	1.74	
$f(^{158}$Gd)	1.41		2.10	5.16	
f(Au)	3.02		4.94	6.79	Uhl
$f(^{152}$Gd)	1.88		3.07	4.78	
$f(^{154}$Gd)	1.37		2.33	3.69	
$f(^{155}$Gd)	0.39		0.89	1.42	
$f(^{156}$Gd)	1.60		2.71	4.28	
$f(^{157}$Gd)	0.67		1.33	2.00	
$f(^{158}$Gd)	2.04		3.52	5.25	
$F_1(^{152}$Gd/Au)	0.988	0.985	0.984	0.982	(Reffo +
$F_1(^{154}$Gd/Au)	0.985	0.979	0.978	0.973	Uhl) / 2
$F_1(^{155}$Gd/Au)	0.979	0.969	0.967	0.954	
$F_1(^{156}$Gd/Au)	0.987	0.981	0.979	0.977	
$F_1(^{157}$Gd/Au)	0.980	0.972	0.970	0.959	
$F_1(^{158}$Gd/Au)	0.990	0.986	0.985	0.984	

The comparison of the two calculations can be summarized by the following points. (i) The calculations of Reffo were performed at 30 keV neutron energy, those of Uhl at 100 keV, thus covering the most important energy range of the present experiment.

(ii) The calculation of Reffo concentrated on the γ-ray cascades. Therefore, corrections for width fluctuation were not considered, which means that absolute cross sections could not be given. In the calculation of Uhl, the model parameters were adjusted to fit the experimental cross section. Therefore these results could be used to extrapolate the measured cross sections to lower neutron energies for the calculation of Maxwellian averaged cross sections (see Sec. VI).

(iii) The comparison of the capture γ-ray spectra of the various gadolinium isotopes shows good agreement between the two calculations of Uhl and Reffo [15]. In case of gold there are more pronounced differences. Here, the harder spectrum obtained by Uhl appears to agree better with experiment [24].

The efficiency of the 4π BaF_2 detector was determined experimentally [25] by measuring the response for monoenergetic γ rays from (p,γ) reactions on thin ^{26}Mg, ^{30}Si, and ^{34}S targets. In these reactions, certain proton resonances decay predominantly by cascades with only two transitions. By replacing one of the BaF_2 modules by a Ge detector, and

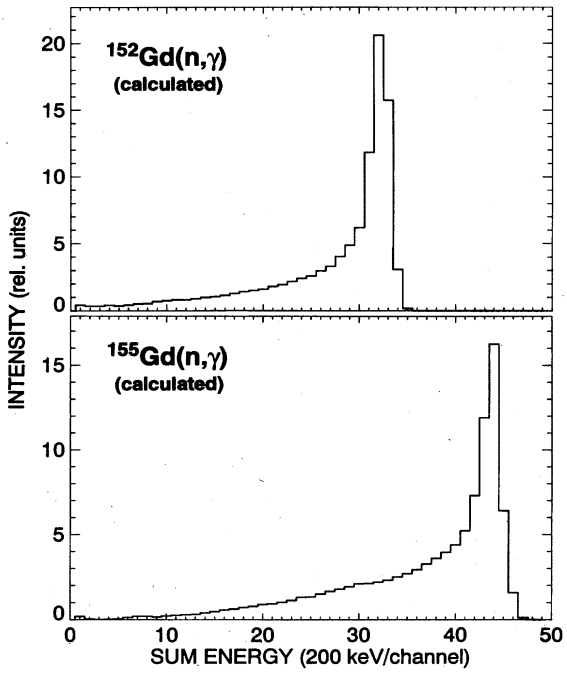

FIG. 7. Calculated sum energy spectra of the $4\pi BaF_2$ detector obtained with the measured line shape for monoenergetic gamma rays. The results for ^{152}Gd and ^{155}Gd are given as examples. These spectra were used to derive the correction F_1 for unobserved capture events.

looking for BaF_2-Ge-coincidences, two-dimensional spectra, E_γ(Ge) versus $E_\gamma(BaF_2)$, were recorded. The response of the 4π BaF_2 detector for monoenergetic γ rays was then obtained by selecting those events, where the full energy of the complementary γ ray is registered in the germanium detector.

Using seven (p,γ) resonances and an ^{88}Y source, the line shapes of 20 γ transitions in the energy range from 0.843 to 8.392 MeV could be determined. These data were used in the calculation of the spectrum fractions, f, and of the correction factors, F_1, given in Table V. The resulting sum energy spectra, which are shown in Fig. 7 for ^{152}Gd and ^{155}Gd, are in good agreement with the experimental spectra of Fig. 5, thus confirming the calculation of the correction factors F_1.

The spectrum fractions, f, obtained with the different sets of capture cascades are compiled in Table V. The values obtained with the cascades of Uhl are systematically larger by $\sim$1.7% for the gold standard, $\sim$1.1% for the even and $\sim$0.2% for the odd gadolinium isotopes. This behavior is expected from the respective calculated γ-ray spectra [15], where the differences for gold spectra are larger than for the gadolinium isotopes. The related systematic uncertainties for the cross section ratios are discussed in detail in Sec. V. The adopted values of the correction factors F_1 in the lower part of Table V are the average of both calculations, except for ^{158}Gd. The small number of capture cascades given by Reffo caused strong fluctuations in the capture γ-ray spectrum and, consequently, in the spectrum fraction f. Since these fluctuations seem to result from numerical effects and are not justified by the systematic trend in the even gadolinium isotopes, only the data of Uhl were used for this isotope.

It is important to note that the improvements of the experimental setup, yielding an increase in solid angle to 96% of 4π, and a reduction of the threshold in sum energy below 1.5 MeV, resulted in a significantly higher detector efficiency than that of Ref. [2]. While the fraction of unobserved capture events in the previous measurements of the samarium and barium cross sections [2,3] was 7% and 6% for the even isotopes, respectively, these values could now be reduced to only 2%.

The capture cascades of Uhl were also used to determine *a posteriori* the correction factors F_1 for the samarium [2] and barium [3] experiments. Again, systematically lower values were obtained compared to the corrections based on the cascades of Reffo. The effect is even more pronounced since the solid angle was lower and the threshold energies significantly higher in the previous experiments. Also in these cases, the differences are again dominated by the gold standard. In summary, the absolute cross sections of the barium and samarium isotopes are lower by 1.5% [3] and by 1.4% [2], respectively. For the individual isotopes, typical deviations from these numbers are $\pm$0.7% and $\pm$0.5% for the barium and samarium families, and thus well within the quoted systematic uncertainties. Since the astrophysical interpretations are essentially based on cross section ratios, they are not affected by these small differences in the absolute values.

The correction for neutron multiple scattering and self-shielding was calculated with the SESH code [18]. The search for consistent parameter sets, which would allow reproduction of the capture cross section *and* the total cross section of each isotope, started with the parameters given by Mughabghab [26], and with the pairing energies from Ref. [27]. These data sets were modified until the measured total cross sections of Table III could be reproduced within their uncertainties and the capture cross sections within $\sim$10%. The final input parameters are listed in Ref. [15] together with the calculated total cross sections. In all calculations, the oxygen content was considered according to the stoichiometry of Gd_2O_3. The resulting correction factors F_2 are given in Table VI.

The corrections for the ^{152}Gd and ^{154}Gd samples required special treatment because of their low isotopic enrichments. In principle, the corrections could be calculated either for the total composition of the sample or for that part which remains after the correction for isotopic impurities. In the present experiment, most samples have about the same size and a weight of $\sim$1.3 g. Therefore the multiple scattering corrections were calculated as though each sample mass was entirely just one of the two main isotopes, ^{152}Gd or ^{154}Gd. Since the samples had very similar masses, quite small, the corrections were only $\sim$2%, on average, except for ^{152}Gd and ^{158}Gd. The related systematic uncertainties are discussed in Sec. V.

IV. RESULTS FOR THE NEUTRON CAPTURE CROSS SECTIONS

The ratios of the neutron capture cross sections of the gadolinium isotopes and of ^{197}Au obtained in the individual runs and via the different evaluation methods are listed to-

TABLE VI. Correction factors for the cross section ratios, $F_2 = \mathrm{MS(Au)/MS}(X)$.

Energy range (keV)	F_2					
	^{152}Gd/Au	^{154}Gd/Au	^{155}Gd/Au	^{156}Gd/Au	^{157}Gd/Au	^{158}Gd/Au
3–5	0.999	1.011	0.988	1.090	0.995	1.258
5–7.5	1.015	1.017	1.005	1.059	1.007	1.145
7.5–10	1.023	1.019	1.014	1.042	1.013	1.113
10–12.5	1.028	1.021	1.019	1.030	1.017	1.083
12.5–15	1.031	1.023	1.021	1.023	1.018	1.069
15–20	1.033	1.024	1.023	1.021	1.018	1.053
20–25	1.035	1.025	1.023	1.018	1.018	1.044
25–30	1.034	1.025	1.021	1.016	1.017	1.038
30–40	1.034	1.025	1.020	1.014	1.015	1.032
40–50	1.033	1.025	1.018	1.012	1.013	1.026
50–60	1.032	1.025	1.017	1.012	1.012	1.022
60–80	1.030	1.024	1.016	1.011	1.010	1.018
80–100	1.029	1.022	1.014	1.010	1.009	1.014
100–120	1.028	1.022	1.013	1.009	1.008	1.012
120–150	1.028	1.021	1.013	1.009	1.008	1.010
150–175	1.027	1.021	1.012	1.008	1.007	1.010
175–200	1.026	1.020	1.011	1.008	1.007	1.009
200–225	1.025	1.019	1.011	1.007	1.007	1.008
Uncertainty (%)	0.7	0.5	0.4	0.4	0.4	0.4

gether with the respective statistical uncertainties in Ref. [15]. The data are free of systematic differences with respect to the different runs or evaluations. This is particularly important for the comparison of runs 1 and 3, which were made with different data acquisition modes.

As in the previous measurements with the 4π BaF_2 detector [1–3], the final cross section ratios were adopted from Evaluation 2. The mean values of the three runs are compiled in Table VII together with the statistical, systematic, and total uncertainties. The energy bins are sufficiently fine to avoid systematic uncertainties in the calculation of the Maxwellian averaged cross sections (Sec. VI). The final uncertainties of the cross section ratios are $\sim 1\%$, a significant improvement compared to previous data [6,21].

The experimental ratios were converted into cross sections using the gold cross section of Macklin [28] after normalization by a factor of 0.989 to the absolute value of Ratynski and Käppeler [29] (Table VIII). The uncertainties of these data can be obtained by adding the 1.5% uncertainty of the reference cross section to the uncertainties of the respective cross section ratios.

The present results for the most important s-only isotopes ^{152}Gd and ^{154}Gd are compared to the data of Beer and Macklin [6] in Fig. 8. These previous data are quoted with an accuracy of 3%, but without considering the systematic uncertainties of the corrections for isotopic impurities. While the results for ^{152}Gd, ^{155}Gd, and ^{157}Gd are in good agreement within the quoted uncertainties, the present ^{154}Gd cross section, which is most important for the astrophysical analysis, is systematically higher by 16% in the relevant energy range from 10 to 100 keV. An older experiment by Shorin *et al.* [30] reported a $\sim 15\%$ higher ^{154}Gd cross section than obtained in this work. A more complete comparison with all existing data will be presented for the stellar cross sections in Sec. VI.

V. DISCUSSION OF UNCERTAINTIES

The determination of statistical and systematic uncertainties in measurements with the 4π BaF_2 detector has been described before in Refs. [1,2,17]. Most of the uncertainties of the gadolinium cross sections are very similar to those of the samarium experiment [2]. Therefore, the following discussion concentrates on the particular aspects of the present study. The various uncertainties are compiled in Table IX.

The isotopic composition is specified by the supplier with an absolute uncertainty of $\pm 0.2\%$. In view of the very good agreement obtained for the samarium isotopes, where the specified isotopic composition was checked by detailed mass spectroscopy [2], this seems to be a conservative estimate. Consequently, the main isotope in the highly enriched samples can be quoted with a relative uncertainty of 0.2%, but because of the low enrichments of the ^{152}Gd and ^{154}Gd samples, relative uncertainties of 0.6% and 0.4% had to be adopted for their isotopic composition, respectively (Table IX).

With the absolute uncertainty of 0.2% in the isotopic composition of Table II, the relative uncertainties due to the even and odd impurity isotopes in the ^{152}Gd sample can both be estimated to be 1%. From the spectrum in Fig. 2 the following contributions to the measured count rate in the relevant region from channels 14 to 82 , that is between threshold and neutron binding energy can be deduced: 47% are from captures in ^{152}Gd, 45% from the odd, and 8% from the even impurity isotopes. The corresponding corrections translate in a systematic uncertainty of 1.0% for the ^{152}Gd spectrum. For ^{154}Gd, the uncertainty of the isotopic correction is 0.6%, while it reduces to 0.2% for all other isotopes.

As noted before, the correction for multiple scattering and self-shielding is also problematic for the samples with low enrichment. The multiple scattering effect may either not be

TABLE VII. Final neutron capture cross section ratios of ^{152}Gd, ^{154}Gd, ^{155}Gd, ^{156}Gd ^{157}Gd, and ^{158}Gd relative to ^{197}Au.

Energy[a] (keV)	$\sigma(^{152}Gd)/\sigma(^{197}Au)$	Uncertainty (%)			$\sigma(^{154}Gd)/\sigma(^{197}Au)$	Uncertainty (%)			$\sigma(^{155}Gd)/\sigma(^{197}Au)$	Uncertainty (%)		
		Stat	Sys	Tot		Stat	Sys	Tot		Stat	Sys	Tot
3–5	1.407	9.1	1.4	9.2	1.389	5.9	1.0	6.0	4.034	5.4	1.0	5.5
5–7.5	1.588	4.3	1.4	4.5	1.361	3.1	1.0	3.3	3.700	2.7	1.0	2.9
7.5–10	1.643	3.9	1.4	4.1	1.604	2.6	1.0	2.8	4.291	2.4	1.0	2.6
10–12.5	1.555	3.1	1.4	3.4	1.494	2.1	1.0	2.3	4.215	1.8	1.0	2.1
12.5–15	1.629	2.7	1.4	3.0	1.572	1.9	1.0	2.1	4.552	1.6	1.0	1.9
15–20	1.690	1.7	1.4	2.2	1.645	1.2	1.0	1.6	4.630	1.0	1.0	1.4
20–25	1.850	1.5	1.4	2.1	1.870	1.0	1.0	1.4	5.018	0.9	1.0	1.3
25–30	1.744	1.3	1.4	1.9	1.827	0.9	1.0	1.3	4.907	0.7	1.0	1.2
30–40	1.748	1.0	1.4	1.7	1.774	0.7	1.0	1.2	4.831	0.6	1.0	1.2
40–50	1.890	1.0	1.4	1.7	1.948	0.7	1.0	1.2	5.136	0.6	1.0	1.2
50–60	1.917	1.0	1.4	1.7	1.949	0.7	1.0	1.2	5.022	0.5	1.0	1.1
60–80	1.955	0.8	1.4	1.6	1.967	0.6	1.0	1.2	4.768	0.5	1.0	1.1
80–100	2.095	0.8	1.4	1.6	2.077	0.6	1.0	1.2	4.708	0.5	1.0	1.1
100–120	2.109	1.0	1.4	1.7	2.066	0.7	1.0	1.2	4.235	0.6	1.0	1.2
120–150	2.240	1.4	1.4	2.0	1.883	1.0	1.0	1.4	3.713	0.9	1.0	1.3
150–175	2.324	1.5	1.4	2.1	1.745	1.1	1.0	1.5	3.398	1.0	1.0	1.4
175–200	2.412	1.5	1.4	2.1	1.668	1.2	1.0	1.6	3.181	1.0	1.0	1.4
200–225	2.572	1.9	1.4	2.4	1.672	1.6	1.0	1.9	3.198	1.3	1.0	1.6

Energy[a] (keV)	$\sigma(^{156}Gd)/\sigma(^{197}Au)$	Uncertainty (%)			$\sigma(^{157}Gd)/\sigma(^{197}Au)$	Uncertainty (%)			$\sigma(^{158}Gd)/\sigma(^{197}Au)$	Uncertainty (%)		
		Stat	Sys	Tot		Stat	Sys	Tot		Stat	Sys	Tot
3–5	0.860	5.6	0.6	5.6	2.234	5.2	0.9	5.3	0.407	7.7	0.6	7.7
5–7.5	0.811	2.9	0.6	3.0	2.071	2.6	0.9	2.8	0.419	3.5	0.6	3.6
7.5–10	0.953	2.5	0.6	2.6	2.384	2.4	0.9	2.6	0.482	3.0	0.6	3.1
10 –12.5	0.880	2.0	0.6	2.1	2.174	1.8	0.9	2.0	0.478	2.2	0.6	2.3
12.5–15	0.941	1.7	0.6	1.8	2.398	1.6	0.9	1.8	0.529	1.9	0.6	2.0
15–20	1.017	1.1	0.6	1.3	2.562	1.0	0.9	1.3	0.577	1.1	0.6	1.3
20–25	1.134	0.9	0.6	1.1	2.697	0.9	0.9	1.3	0.665	1.0	0.6	1.2
25–30	1.071	0.8	0.6	1.0	2.610	0.7	0.9	1.1	0.603	0.8	0.6	1.2
30–40	1.124	0.6	0.6	0.8	2.578	0.6	0.9	1.1	0.615	0.6	0.6	0.8
40–50	1.219	0.6	0.6	0.8	2.711	0.6	0.9	1.1	0.636	0.6	0.6	0.8
50–60	1.225	0.6	0.6	0.8	2.590	0.6	0.9	1.1	0.638	0.6	0.6	0.8
60–80	1.181	0.5	0.6	0.8	2.212	0.5	0.9	1.0	0.641	0.5	0.6	0.8
80–100	1.184	0.5	0.6	0.8	1.980	0.5	0.9	1.0	0.521	0.6	0.6	0.8
100–120	1.061	0.6	0.6	0.8	1.830	0.6	0.9	1.1	0.460	0.7	0.6	0.9
120–150	0.951	0.9	0.6	1.1	1.611	0.9	0.9	1.3	0.406	1.0	0.6	1.2
150–175	0.875	1.0	0.6	1.2	1.444	1.0	0.9	1.3	0.355	1.2	0.6	1.3
175–200	0.811	1.1	0.6	1.3	1.350	1.0	0.9	1.3	0.352	1.2	0.6	1.3
200–225	0.798	1.4	0.6	1.5	1.330	1.4	0.9	1.7	0.346	1.6	0.6	1.7

[a]Energy intervals chosen for calculating the Maxwellian averaged cross sections.

completely considered or even overcompensated by subtracting the normalized spectra of the impurity isotopes. On average, the various contributions of the isotopic impurities will compensate each other. Therefore, the correction was calculated for the final spectra after subtraction of the isotopic impurities. In order to estimate the related systematic uncertainty, the extreme case of the uncorrected spectra was investigated as well. The respective differences were 2.4% and 1.6% for the ^{152}Gd and ^{154}Gd samples, nearly independent of neutron energy. Therefore, 25% of this difference were adopted as a reasonable estimate for the related systematic uncertainty, in addition to the 0.4% uncertainty generally considered for the pure isotopes.

The systematic uncertainties of the corrections for undetected events, F_1, were estimated from the differences obtained with the capture cascades of Reffo and of Uhl. While the differences in the spectrum fractions, f, are sizable (Sec. III), this problem is greatly reduced for the cross section ratios. Hence the correction factors, F_1, showed mean deviations of only $\pm 0.3\%$ for the even and of $\pm 0.8\%$ for the odd isotopes. These differences were assumed as the related systematic uncertainties. That the uncertainties for the even iso-

TABLE VIII. Neutron capture cross sections of ^{152}Gd, ^{154}Gd, ^{155}Gd, ^{156}Gd, ^{157}Gd, and ^{158}Gd.

Energy interval[a] (keV)	$\sigma(^{197}\text{Au})$ [b] (mb)	$\sigma(^{152}\text{Gd})$ (mb)	$\sigma(^{154}\text{Gd})$ (mb)	$\sigma(^{155}\text{Gd})$ (mb)	$\sigma(^{156}\text{Gd})$ (mb)	$\sigma(^{157}\text{Gd})$ (mb)	$\sigma(^{158}\text{Gd})$ (mb)
3–5	2266.7	3190	3148	9145	1949	5063	923.1
5–7.5	1726.7	2742	2350	6388	1401	3576	722.7
7.5–10	1215.7	1998	1949	5217	1158	2898	586.2
10–12.5	1066.7	1659	1593	4496	938.3	2319	509.8
12.5–15	878.0	1430	1380	3997	826.3	2105	464.7
15–20	738.8	1248	1215	3420	751.1	1893	426.4
20–25	600.0	1110	1122	3011	680.5	1618	399.2
25–30	570.8	995.2	1043	2801	611.2	1490	344.0
30–40	500.4	874.9	887.5	2417	562.6	1290	307.9
40–50	433.3	818.9	844.3	2225	528.3	1175	275.7
50–60	389.6	746.9	759.5	1957	477.5	1009	248.7
60–80	349.4	683.2	687.1	1666	412.7	772.9	223.9
80–100	298.3	624.8	619.6	1404	353.1	590.7	155.5
100–120	290.1	611.9	599.4	1229	307.9	530.9	133.4
120–150	274.1	614.0	516.1	1018	260.7	441.7	111.3
150–175	263.7	612.7	460.0	895.9	230.6	380.6	93.68
175–200	252.6	609.2	421.3	803.3	204.9	340.9	88.86
200–225	248.5	639.1	415.3	794.5	198.3	330.5	86.07

[a]Chosen for calculating the Maxwellian averaged cross sections.
[b]Based on the ^{197}Au data from literature [28,29].

topes are significantly smaller than in previous experiments with the 4π BaF_2 detector is the direct consequence of improving the efficiency from ~95 to 98%. The comparably large uncertainty for the odd isotopes results from the differences in the calculations for the gold sample. However, this problem affects only the cross section ratios relative to gold, whereas the ratios of two gadolinium isotopes can be given with significantly better accuracy. The systematic uncertainties in the ratio of two even isotopes are only 0.15%, those for the ratios of an odd and an even isotope are 0.45%.

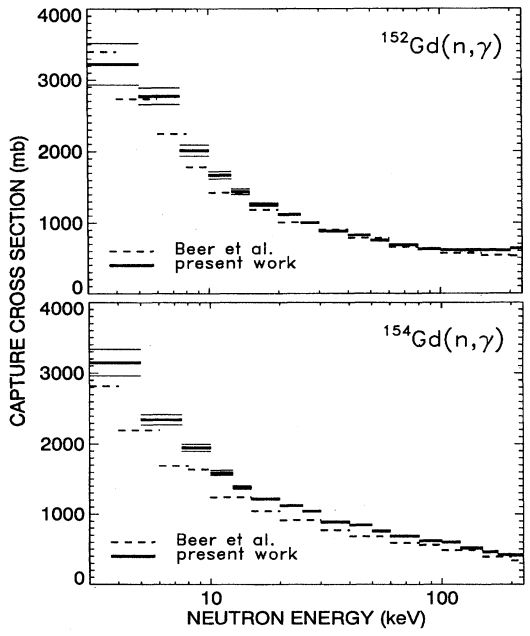

FIG. 8. The neutron capture cross sections of ^{152}Gd and ^{154}Gd compared to the data of Beer and Macklin (Ref. [6]).

VI. MAXWELLIAN AVERAGED CROSS SECTIONS

Maxwellian averaged cross sections were calculated in the same way as described in Refs. [1,17], the results are given in Table X. The neutron energy range from 0 to 700 keV was divided into three intervals according to the origin of the adopted cross sections. The respective contributions I_x are given in detail in Ref. [15]. The main contributions from the interval I_2 are provided by the present experiment, which covered the energy range from 3 to 225 keV. This

TABLE IX. Systematic uncertainties (%).

Flight path		0.1
Neutron flux normalization		0.2
Sample mass (impurity elements)		0.2
Isotopic composition (^{152}Gd/^{154}Gd/^{15x}Gd [a] samples)		0.6/0.4/0.2
Isotopic correction (^{152}Gd/^{154}Gd/^{15x}Gd [a] samples)		1.0/0.6/0.2
Multiple scattering and self-shielding: F_2 (^{152}Gd/^{154}Gd/^{15x}Gd [a] samples)		0.7/0.5/0.4
Undetected events: F_1		
even Gd isotopes		0.3
odd Gd isotopes		0.8
Total systematic uncertainties		
	$\sigma(^{152}\text{Gd})/\sigma(\text{Au})$	1.4
	$\sigma(^{154}\text{Gd})/\sigma(\text{Au})$	1.0
	$\sigma(^{155}\text{Gd})/\sigma(\text{Au})$	1.0
	$\sigma(^{156}\text{Gd})/\sigma(\text{Au})$	0.6
	$\sigma(^{157}\text{Gd})/\sigma(\text{Au})$	0.9
	$\sigma(^{158}\text{Gd})/\sigma(\text{Au})$	0.6

[a]x stands for the numbers 5, 6, 7, and 8.

TABLE X. Maxwellian averaged neutron capture cross sections of ^{152}Gd, ^{154}Gd, ^{155}Gd, ^{156}Gd, ^{157}Gd, and ^{158}Gd for thermal energies from 10 to 100 keV. (The 1.5% uncertainty of the gold standard is not included here, since it cancels out in most applications of relevance for nuclear astrophysics.)

kT (keV)	^{152}Gd (mb)	^{154}Gd (mb)	^{155}Gd (mb)	^{156}Gd (mb)	^{157}Gd (mb)	^{158}Gd (mb)
10	1951±49	1863±38	5030±93	1117±20	2803±56	595.4±11
12	1732±38	1668±30	4507±74	1004±15	2487±42	538.2±8.4
20	1280±23	1258±16	3347±42	760.4±7.6	1791±22	407.6±4.2
25	1142±19	1124±14	2943±34	676.8±6.0	1547±17	359.8±3.3
30	1049±17	1028±12	2648±30	615.2±5.1	1369±15	323.6±2.8
40	933.1±15	897.7±9.8	2233±24	528.0±4.0	1123±11	271.5±2.1
50	864.4±14	809.5±8.8	1948±21	468.0±3.6	958.8±9.5	235.5±1.8
52	853.6±13	795.1±8.6	1902±21	458.2±3.4	932.3±9.3	229.7±1.8
60	818.0±12	744.5±8.1	1738±19	424.1±3.2	841.1±8.3	209.3±1.6
70	783.6±13	694.0±7.7	1574±18	390.3±3.0	752.3±7.6	189.5±1.5
80	756.3±13	653.4±7.7	1441±16	363.9±3.1	682.7±7.1	174.2±1.5
90	733.1±13	620.0±7.8	1332±15	342.5±3.4	626.6±6.8	161.8±1.6
100	712.3±13	591.4±8.2	1238±15	324.5±3.6	580.3±6.6	151.6±1.6

range accounts for 96% of the stellar cross section at $kT=30$ keV and ~85% at $kT=10$ keV. The present data are provided with sufficient resolution to avoid systematic uncertainties that may result from a coarse energy grid.

The contributions I_1 from the energy range from 0 to 3 keV were determined in three different ways. First, the cross section energy dependencies from statistical model calculations were fitted to the present results and to the data that were calculated from resonance parameters at lower energies [26,31]. In a second calculation, the cross sections of the Joint Evaluated File [19] were normalized to the present data between 3 to 10 keV. The respective normalization factors were less than ~20% except for ^{152}Gd, where a factor of 2 was required. Finally, this procedure was repeated using the calculated cross sections of Uhl. The adopted values for the contributions I_1 are the averages of these three calculations. The quoted uncertainties of 10% correspond to the observed differences from the mean, and include the respective systematic uncertainties.

The energy interval from 225 to 700 keV contributes very little to the Maxwellian average at typical s-process temperatures. There, the JEF data [19] were normalized to the present results between 100 to 200 keV. The uncertainties were calculated under the assumption that the uncertainties of the normalized cross sections increase from 2% at 225 keV to 10% at 700 keV neutron energy.

The present results at $kT=30$ keV are eventually compared in Table XI with previous experiments and with the compilations of Bao and Käppeler [21] and Beer, Voss, and Winters [32]. While the individual results are in fair agreement within the quoted uncertainties for ^{152}Gd, ^{155}Gd, ^{156}Gd, and ^{157}Gd, significant differences are found for ^{154}Gd and ^{158}Gd. In all cases, the uncertainties have been reduced significantly by the present experimental technique.

VII. ASTROPHYSICAL IMPLICATIONS

A. The s-process branchings between ^{150}Sm and ^{156}Gd

The s-process reaction flow in the Sm-Eu-Gd region exhibits a number of branching points as indicated in Fig. 1. The strength of these branchings is defined by the abundances of the s-only isotopes ^{152}Gd and ^{154}Gd, which are shielded against the β-decay chains from the r-process region by their samarium isobars.

Since the rare earth elements are chemically nearly identical, their abundance ratios are known to ±1.3% on average [5]. Hence the following analyses can be normalized via the unbranched s-only isotope ^{150}Sm. This allows us to treat the branchings to ^{152}Gd and ^{154}Gd independent of each other, referring each to ^{150}Sm. Compared to the previous analysis of Beer and Macklin [6], which concentrated on the ^{152}Gd/^{154}Gd ratio, this offers the advantage of separating the effects due to the stellar β decay rates of the branch point nuclei from the p-process corrections and from a possible enhancement of the stellar neutron capture rate of ^{154}Gd (see below).

The resulting s abundances of ^{152}Gd and ^{154}Gd are mainly determined by the branching points ^{151}Sm and ^{154}Eu. The branching at ^{155}Eu is required for determining the s-process abundance of ^{155}Gd, an important test for the identification of pure s-process gadolinium that may be discovered in meteoritic material. The additional branchings at ^{152}Eu and ^{153}Gd are too weak to produce a noticeable effect on the abundance pattern.

Since the decay rates of the main branch point nuclei exhibit a significant temperature dependence, these branchings can be analyzed in terms of the s-process temperature. The determination of the branching factors

$$f_\beta=\frac{\lambda_\beta}{\lambda_\beta+\lambda_n}, \tag{2}$$

requires the stellar rates for β decay, λ_β, and for neutron capture, λ_n. Most of these data are related to the nuclear properties of the involved nuclei and are discussed in the following section. Only the neutron density has to be determined independently, either by analysis of complementary branchings, which are insensitive to temperature, or directly from a stellar model of the s-process site as described in the section on model calculations.

TABLE XI. Maxwellian averaged cross sections at $kT=30$ keV compared to previous experiments and evaluations.

	Experiment		Evaluation	
Isotope	Cross section (mb)	Reference	Bao and Käppeler [21]	Beer, Voss, Winters [32]
^{152}Gd	1049±17	Present work [a]	985 ± 61	1045 ± 65
	1003±30	Beer and Macklin [6]		
	997±62	Beer *et al.* [33]		
^{154}Gd	1028±12	Present work [a]	1278±102	878±27
	878±27	Beer and Macklin [6]		
	1184±94	Shorin *et al.* [30]		
^{155}Gd	2648±30	Present work [a]	2800±280	2721±90
	2990±150	Nakajima *et al.* [34]		
	2721±90	Beer and Macklin [6]		
	2595±260	Shorin *et al.* [30]		
^{156}Gd	615.2±5.1	Present work [a]	639±64	639±64
	592±59	Kononov *et al.* [35]		
^{157}Gd	1369±15	Present work [a]	1538±154	1355±39
	1366±70	Nakajima *et al.* [34]		
	1355±39	Beer and Macklin [6]		
	1425±142	Shorin *et al.* [30]		
^{158}Gd	323.6±2.8	Present work [a]	208±19	221±20
	304±20	Bokhovko *et al.* [36]		
	211±19	Beer *et al.* [33]		
	392±39	Kononov *et al.* [35]		
	477±292	Thirumala *et al.* [37]		
	523±60	Stupegia *et al.* [38]		

[a]The 1.5% uncertainty of the gold cross section is not included here, since it cancels out in most applications of relevance for nuclear astrophysics.

B. Input data

Cross sections. The most important data for defining the branchings of Fig. 1 are the stellar cross section ratios of the s-only nuclei ^{152}Gd and ^{154}Gd determined in this work, and of ^{150}Sm [2], which are now known to ±1%. The total s-process flow is characterized by the $\langle\sigma\rangle N_s$ value of the unbranched isotope ^{150}Sm (the product of stellar cross section times the s-process abundance), while the effect of the branchings can be expressed by the $\langle\sigma\rangle N_s$ ratios of ^{152}Gd and ^{154}Gd relative to ^{150}Sm.

The cross sections of the remaining stable isotopes, ^{152}Sm, ^{151}Eu, and ^{153}Eu are adopted from Refs. [2,39], but have relatively little impact for the branching analyses. In contrast, the cross sections for the main branch point isotopes are crucial for the reaction flow. For ^{151}Sm, the calculated value of Ref. [40] could be adopted, which is based on a carefully evaluated local parameter systematics. Since this cross section is still affected by the 25% uncertainty inherent to the statistical model, an experimental determination (which appears feasible with existing techniques [41]) would be highly desirable.

For ^{154}Eu the situation is worse. The available data are summarized in Fig. 9, which illustrates the evaluation of the

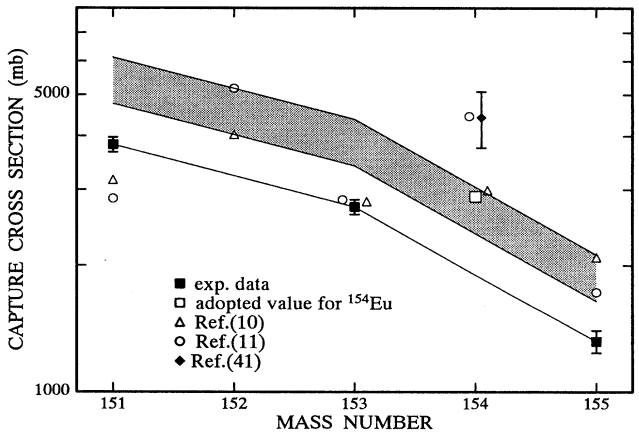

FIG. 9. The stellar (n,γ) cross sections at $kT=30$ keV of the europium isotopes. Experimental and calculated values are indicated by solid and open squares, respectively. Based on this systematics, a value of 2900 mb was adopted for ^{154}Eu in addition to the 4420±663 mb from Ref. [43].

values adopted here. Reliable experimental cross sections (solid squares) are known for the stable isotopes ^{151}Eu and ^{153}Eu [39] as well as for the unstable branch point ^{155}Eu [42]. The existing statistical model calculations [12,13] (open symbols) are in agreement with these values, at least within their quoted uncertainties of 50%. If the cross section trend with mass number of the experimental values is adopted for the odd-odd isotopes as well, the shaded band describes a range of plausible values, which fits quite well with the average (open square) obtained by normalization of the calculated cross section sets to the experimental data. However, this value of 2900 mb is much smaller than an integral cross section value of 4420 ± 663 mb measured in a fast reactor [43]. Therefore, both values were used in the present branching analysis.

Another serious uncertainty refers to a possible stellar enhancement of the ^{154}Gd cross section due to the population of low-lying excited nuclear states in the thermal photon bath. If the population probabilities are high enough, such an enhancement may result from differences in the neutron capture cross sections of ground state and excited states. This effect has been considered in the calculations of Harris [12] and of Holmes *et al.*, [13] leading to enhancement factors of 10% and 1% at $kT = 30$ keV, respectively. In view of this discrepancy, no correction for this effect was made, but it should certainly be addressed in future studies.

Beta decay rates. The stellar beta decay rates were adopted from the tables of Takahashi and Yokoi [4]. These rates were evaluated for complete thermal equilibrium between the ground state and the excited nuclear states, an assumption that is satisfied for all unstable nuclei of interest here. It holds, in particular for ^{152}Eu, where the stellar half-life is determined by the short-lived isomer rather than by the ground state. Apart from temperature effects, there is also a (weaker) influence of electron density on the relevant decay rates, except for ^{153}Sm and ^{154}Eu. In all cases, where β^- decay competes with β^+ or EC decay, the β^- channel is much faster.

Abundances. The s-process calculations presented in the following were normalized to the solar abundance of ^{150}Sm. Though the solar abundances of Sm, Eu, and Gd are given with uncertainties of only 1.3%, 1.6%, and 1.4% (Anders and Grevesse [5]), an additional uncertainty arises from possible p-process contributions to the abundances of the s-only isotopes. An empirical estimate based on the abundances of nearby p-only isotopes suggests a large correction for ^{152}Gd of up to 50% [6]. However, improved calculations [7,8,44] have reported p-process yields of less than 12% for this isotope. Another contribution to the ^{152}Gd abundance comes from the s process in massive stars, which is estimated to account for about 6% of the solar value [9]. Fortunately, the p-process yields for ^{154}Gd and ^{150}Sm are much smaller (below 1.5% and 0.2%, respectively [45]) and, therefore, less critical.

Apart from the p-process corrections, there is also the problem of mass fractionation in the experimental determination of the isotopic composition [46]. This difficulty refers to the composition of solar gadolinium as well as to that of the enriched samples. Presently, the related corrections are still unknown, but a conservative assessment suggests an additional uncertainty of 0.6% for the isotopic ratio of ^{152}Gd and ^{154}Gd due to mass fractionation.

C. s-process models

Analyses of the s-process reaction flow in the Sm-Eu-Gd region were carried out by means of the classical approach as well as by a stellar model for helium shell burning in low mass stars. Only a brief sketch of these models is given here since a more detailed description can be found elsewhere [47].

The—purely phenomenological—classical approach has been formulated before stellar models for the helium burning stage were available [48,49]. Since then, it became a useful tool, not only for reproducing the s abundances but also for characterizing the physical conditions during the s process in an empirical way. Meanwhile, the two components of the classical approach could be assigned to stellar scenarios. The *weak* component, which is important in the mass range between Fe and Zr, was attributed to helium core burning in massive stars [9], while the *main* component occurs during helium shell burning in low mass stars and accounts for the s abundances in the mass range $A > 100$. For the main component, irradiation of an iron seed by an exponential distribution of neutron exposures was assumed. With the further assumption of a constant neutron density and temperature, the s-process reaction flow is characterized in this approach by the iterative expression

$$\langle\sigma\rangle N_s(A) = \frac{G N_\odot^{56}}{\tau_0} \prod_{i=56}^{A} \left(1 + \frac{1}{\sigma_i \tau_0}\right)^{-1} . \qquad (3)$$

The two free parameters, the fraction G of the observed ^{56}Fe abundance required as seed, and the mean neutron exposure τ_0, are determined by fitting the empirical $\langle\sigma\rangle N_s$ values of those s-only isotopes that experience the entire reaction flow. For the present analysis,

$$\tau_0 = (0.303 \pm 0.010)\left(\frac{kT[\text{keV}]}{30}\right)^{1/2} \text{ mb}^{-1}, \qquad (4)$$

has been adopted from Ref. [2], whereas G was defined by normalization to the $\langle\sigma\rangle N_s$ value of ^{150}Sm.

Branchings in the s-process path have to be treated separately [50,47] via the branching factors defined by Eq. (2). The adopted half-lives and Maxwellian averaged cross sections are discussed above, and the neutron density, $n_n = (4.1 \pm 0.6)\ 10^8$ cm^{-3}, was taken from Ref. [40].

The combined effect of the branchings in Fig. 1 can be deduced from the $\langle\sigma\rangle N_s$ ratios of the partially bypassed s-only isotopes ^{152}Gd and ^{154}Gd relative to ^{150}Sm, which is exposed to the entire s-process flow. Since the neutron density is defined by the branchings in the neodymium/promethium region, reproduction of the ^{152}Gd and ^{154}Gd abundances requires the proper choice of the effective stellar temperature via the temperature-dependent β-decay rates of the branch point isotopes, mainly of ^{151}Sm and ^{154}Eu.

The only stellar model for describing the s process in the mass range $A > 100$ in a satisfactory way has been suggested by Iben and Renzini [51,52] for helium shell burning in low mass stars (LMS). This model was shown to reproduce successfully the s-process abundances by the operation of two

neutron sources during a series of subsequent helium shell flashes [10,11,47]. First, the $^{13}C(\alpha,n)^{16}O$ reaction occurs by ingestion of a ^{13}C pocket into the convective helium burning zone, giving rise to more than 90% of the neutron exposure, followed by a second burst of neutrons from the ^{22}Ne $(\alpha,n)^{25}Mg$ reaction. Both neutron sources work at different temperatures and neutron densities. The ^{13}C source lasts for typically 20 yr at a thermal energy of 12 keV producing neutron densities of a few times 10^8 cm^{-3}. After an interpulse period of ~20 yr, the ^{22}Ne source burns for about 3 yr when thermal energies around 26 keV are reached at the end of the helium burning episode. Then follows a period of hydrogen shell burning, which takes some 10^5 yr to replenish the consumed helium for the next shell flash to start. These shell flashes may occur up to 20 times.

The pulsed nature of this model implies additional parameters compared to the classical case: the gradients in neutron density and temperature for each burst as well as the respective time scales. It is important to note that pulse durations and interpulse periods have negligible influence on the abundances of the branchings discussed here because the neutron capture cross sections in this mass region are large enough that typical neutron capture times are significantly shorter than the duration of the neutron exposures. Hence there is ample time to readjust the abundance pattern in the ^{22}Ne phase, regardless of the situation after the ^{13}C phase. Therefore, the temperature measured by the $A=151-154$ branchings corresponds to that at the end of the He shell flash when the ^{22}Ne source is activated.

Accordingly, the branchings to ^{152}Gd and ^{154}Gd are not sensitive to a recent modification of the LMS model by Straniero *et al.* [53], who discovered a considerable modification with respect to the ^{13}C source. Instead of waiting in the radiative envelope until being engulfed by the convective He burning shell, the ^{13}C synthesized at the H/He interface during the interpulse period is completely burnt in the radiative environment. Since this occurs at a lower temperature corresponding to $kT=8$ keV, the related neutron densities are restricted to a few 10^7 cm^{-3}. This difference to the first LMS model has practically no consequences for the final abundances, which are dominated by the characteristics of the ^{22}Ne phase.

D. Results and discussion

The results obtained with the classical approach are indicated in Table XII for different choices of thermal energy and electron density. The last two lines in Table XII refer to the abundance contributions from alternative production sites, which provide a non-neglible fraction of ^{152}Gd. Though not very efficient in the mass range $A>100$, the s-process in massive stars was shown to account for about 6% of the rare ^{152}Gd [9]. This value corresponds to the final ^{152}Gd abundance including the carbon burning phase, which causes a depletion of the ^{152}Gd synthesized earlier during the helium burning phase (~40% for a 25 $M_\odot$ star). The quoted p-process abundances are from model calculations for Ne/O burning in supernovas of type II (SNII) [45,44]. These calculations start from an initial s-process abundance distribution due to helium core burning in the (massive) SNII precursor, but without considering any modification during the intermediate carbon burning phase. Therefore, the p-process contribution to ^{152}Gd of 12% should rather be taken as an upper limit. In total, only about 80% of the solar ^{152}Gd but practically all of the ^{154}Gd should be accounted for by the main s-process component.

TABLE XII. ^{152}Gd and ^{154}Gd abundances from classical approach.

Run	$N_s(^{152}Gd)$ [a]	$N_s(^{154}Gd)$ [b]	Comment [c]
*n*35*t*29*e*20 [d]	0.463 (70%)	6.782 (94%)	(+)
*n*47*t*29*e*20	0.347 (53%)	6.522 (91%)	–
*n*35*t*32*e*20	0.598 (91%)	6.935 (97%)	(–)
*n*47*t*32*e*20	0.456 (69%)	6.700 (93%)	(–)
*n*35*t*29*e*29	0.435 (66%)	6.753 (94%)	+
*n*47*t*32*e*29	0.436 (66%)	6.705 (93%)	+
	<12%	<2%	*p* process
	~6%		Massive stars

[a]All abundances times 1000.
[b]Including the decay of ^{154}Eu and using a stellar ^{154}Eu cross section of 2900 mb at $kT=30$ keV.
[c]Acceptable (+) or inconsistent (–) solutions.
[d]($n_n=3.5\times 10^8$ cm^{-3}, $kT=29$ keV, $n_e=2.0\times 10^{27}$ cm^{-3}.)

The upper part of Table XII shows the s abundances obtained with the classical approach and using the smaller stellar cross section for ^{154}Eu of 2900 mb at 30 keV thermal energy. First, the results obtained with the previous best estimates for neutron density [$n_n = (4.1\pm0.6)\ 10^8$ cm^{-3} [40]], thermal energy ($kT=29$ keV [47]), electron density ($n_e=2.0\ 10^{27}$ cm^{-3} [54]) are presented (lines 1 and 2). Obviously, an acceptable solution exists only for the lower limit of the neutron density range. Increasing the temperature (lines 3 and 4) seems to improve the agreement with the solar abundances. However, these parameters are in conflict with the nearby branching at $A=163$, where they cause an overproduction of ^{164}Er [55]. This problem can only be removed if the electron density is raised by 50% as well (lines 5 and 6).

If the larger ^{154}Eu cross section of 4420 ± 66 mb is adopted, these analyses yield a ^{154}Gd abundance which is lower by typically 9% compared to the values in Table XII.

The results of Table XII can be summarized in four points.

(i) With the present cross section data, the acceptable range of thermal energies could be reduced to $28<kT<33$ keV, which represents a significant improvement compared to the previously reported interval of 29 ± 5 keV [47].

(ii) The electron density has little influence on the branchings to ^{152}Gd and ^{154}Gd (lines 1 and 5), but it is important for the branching to ^{164}Er.

(iii) The acceptable solutions suggest that only 70% of ^{152}Gd are produced by the main s-process component. The remaining 30% must be ascribed to other processes, but are not completely accounted for by the weak s-process component from massive stars [9] and by the p process in supernovas of type II [44].

TABLE XIII. s abundances and r-process residuals of the gadolinium isotopes.

		Classical approach[b]		LMS model[b,c]
Isotope	$N_\odot$[a]	N_s[d]	$N_r = N_\odot - N_s$	N_s[d]
^{150}Sm	19.1±0.25	19.10±0.25		19.1
^{152}Sm	68.9±0.90	15.94±0.35	53.0±1.0	15.6
^{154}Sm	58.6±0.76		58.6±0.8	
^{153}Eu	50.8±0.81	2.92±0.13	47.9±0.8	2.95
^{152}Gd	0.66±0.009	0.44±0.05		0.88
^{154}Gd	7.19±0.10	6.73±0.55		6.91
^{155}Gd	48.8±0.68	3.30±0.30	45.5±0.8	2.93
^{156}Gd	67.6±0.95	12.87±0.15	54.7±1.0	12.5
^{157}Gd	51.6±0.72	5.77±0.06	45.8±0.8	5.46
^{158}Gd	82.0±1.15	24.17±0.25	57.8±1.2	23.6

[a]All abundances times 1000.
[b]Calculated with a stellar ^{154}Eu cross section of 2900 mb at $kT=30$ keV.
[c]The larger cross section of Ref. [43] gives a 7% smaller ^{154}Gd abundance, all other changes being $\leq 2\%$.
[d]Including the decay of isobars.

(iv) The ^{154}Gd abundance can be reproduced by the main s-process component to 94% or 85% depending on whether the smaller or larger ^{154}Eu cross section is used in the analysis. This deficiency becomes even larger if the stellar enhancement of the (n,γ) rates due to captures in excited states is considered as well. Although the predicted effects from the calculations of Harris [12] and Holmes *et al.* [13] are in conflict for ^{154}Eu and ^{154}Gd, enhancement factors of about 10% at a thermal energy of $kT=30$ keV appear to be possible. Therefore, these effects require verification since they are important for the final s-process yield of ^{154}Gd.

The gadolinium abundances obtained with both s-process models and the resulting r-process residuals are summarized in Table XIII.

The s abundances resulting from the LMS model were calculated with the network code NETZ [56] using the profiles for neutron density, temperature, and electron density from the work of Gallino *et al.* [57]. Contrary to most other branchings, there are significant differences in the gadolinium yields compared to the classical approach. The abundance evolution during a helium shell flash is plotted in Fig. 10 for the investigated s-only nuclei together with the neutron density profiles from the ^{13}C and the ^{22}Ne sources.

The unbranched isotope ^{150}Sm shows a very smooth abundance buildup during the ^{13}C phase, which is decreasing due to the later mixing with unprocessed material when the convective helium shell is progressing beyond the ^{13}C pocket. The different pattern obtained for the two Gd isotopes results from the temperature dependence of the preceding branch points. The smaller β-decay rates at the lower temperature during the ^{13}C phase are favoring the neutron capture part of the branchings, so that more of the reaction flow is bypassing ^{152}Gd and ^{154}Gd. This depletion during the ^{13}C phase is followed by an increase due to mixing with unprocessed material as the shell flash progresses beyond the ^{13}C pocket. In between the ^{13}C phase, and the ^{22}Ne phase,

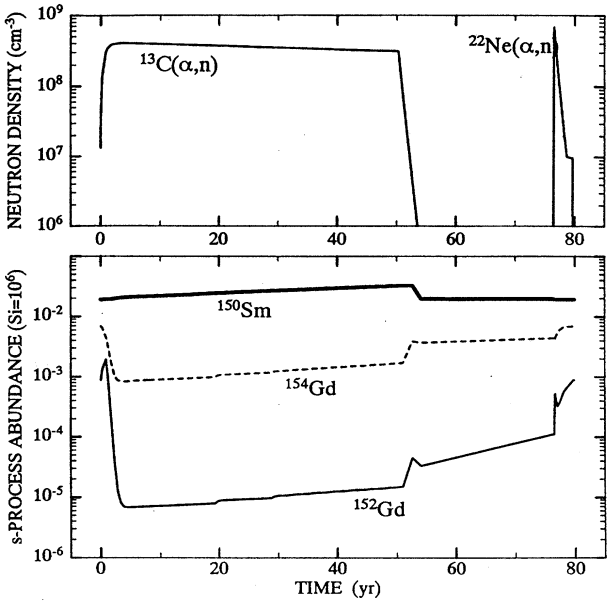

FIG. 10. The abundance evolution of the s-only isotopes during a helium shell flash. The neutron density profiles are shown in the upper part.

the ^{152}Gd abundance increases further due to the decay of ^{152}Eu.

The second exposure by the ^{22}Ne reaction at the end of the helium shell flash has a different effect on the two Gd isotopes. The ^{154}Gd abundance shows a smooth increase and stabilizes at 96% or 89% of the solar abundance, depending on whether the smaller or the larger ^{154}Eu cross section is adopted. Since the temperature during neutron freeze-out is already lower than during the maximum, the stellar cross section enhancement is less important in this model. The most severe problem for the stellar model is, however, that ^{152}Gd is overproduced by 33%. Instead of stabilizing at a certain value, the ^{152}Gd abundance exhibits an interesting behavior during the ^{22}Ne phase. In the beginning, it follows the neutron density profile almost instantaneously, since the ^{151}Sm branching is activated by the higher temperature. This close correlation confirms that the branching is not sensitive to pulses longer than a few months. However, freeze-out seems to be very important: Even after the ^{151}Sm branching was deactivated due to the decreasing temperature, the ^{152}Gd abundance continues to increase as a result of neutron captures on the remaining ^{151}Eu. This further ^{152}Gd production during freeze-out is favored by the large ^{151}Eu cross section.

That the final ^{152}Gd yield is indeed determined by freeze-out can be seen at the beginning of the ^{13}C exposure. At first, the ^{152}Gd abundance continues to increase until the ^{151}Eu reservoir of the preceding helium shell flash is exhausted. Only then, it drops to the level corresponding to the reduced ^{151}Sm branching probability at the lower temperature. This result means that the ^{152}Gd production can be used to probe the profiles for neutron density and temperature during helium shell burning.

The revised LMS model where the ^{13}C source burns under radiative conditions at $kT=8$ keV shows essentially the same significant overproduction of ^{152}Gd (37% according to Refs. [53,57]). This is not surprising since the decisive neutron burst from the ^{22}Ne source is unchanged.

Table XIII shows that the two models differ also with respect to the s abundance of ^{155}Gd. In view of the much smaller cross section uncertainties, this 13% difference is sufficiently significant to provide an important test if s-only gadolinium can be isolated from meteoritic material.

VIII. SUMMARY

The Karlsruhe 4π Barium Fluoride Detector has been improved by replacing the six crystals with the highest α background and by adding a pierced crystal in the zero degree position at the exit of the neutron beam. These changes allowed to reduce the electronic threshold to 1.5 MeV in the γ-ray spectrum and to cover a solid angle of 96% of 4π. In this way, overall detection probabilities of 98% and 99% could be reached for neutron captures in for the even and odd Gd isotopes, respectively.

The total cross sections and the (n,γ) cross sections were measured for the stable isotopes ^{152}Gd, ^{154}Gd, ^{155}Gd, ^{156}Gd, ^{157}Gd, and ^{158}Gd. The total cross sections could be determined from 10 to 200 keV with typical uncertainties from 5 to 25%, depending on the required correction for isotopic impurities. The neutron capture cross sections were measured from 3 to 225 keV. In this case, corrections for the large isotopic impurities of the ^{152}Gd and ^{154}Gd samples could be made with much better accuracy due to the spectroscopic features of the BaF_2 detector. Maxwellian averaged (n,γ) cross sections were derived for thermal energies from 10 to 100 keV. The astrophysically relevant cross section ratios could be determined with an overall uncertainty of typically 1%, an improvement by factors of 5 to 10 compared to existing data. Severe discrepancies were found with respect to previous results.

An updated analysis of the s-process reaction flow in the mass region $150 < A < 160$ was performed on the basis of the Gd cross sections presented here and with additional experimental information on the Eu isotopes. This mass region is important because of the temperature-dependent branchings at ^{151}Sm, ^{154}Eu, and ^{155}Eu. Two s-process models were applied, the classical approach and a stellar model for helium shell burning in low mass stars. The empirical feature of the classical approach could be used to constrain the effective s-process temperature to a range of thermal energies between $kT=28$ keV and 33 keV without overproducing the s-only isotopes.

The LMS model was found to suffer from a significant overproduction of ^{152}Gd by 33% which persists also after a revision of this scenario with respect to neutron density and temperature during the operation of the ^{13}C neutron source. This overproduction was shown to depend strongly on the neutron freeze-out at the end of the helium shell burning episodes, so that the ^{152}Gd abundance might be used to probe this effect.

Remaining problems for further s-process discussions of the mass region between samarium and gadolinium are the improvement of the stellar cross sections for the branch points ^{151}Sm and ^{154}Eu. Another important point is to study the possible stellar enhancement of the ^{154}Eu and ^{154}Gd cross sections. Such an investigation should include the unbranched s-only isotope ^{160}Dy, where this effect can be tested by comparison of the empirical $\langle\sigma\rangle N_s$ value with the overall systematics. The availability of accurate cross sections for the Gd isotopes would certainly justify a renewed search for isotopic anomalies in order to check the present analyses with pure s-process material.

ACKNOWLEDGMENTS

We would like to thank F.H. Fröhner and B. Krieg for providing us with the JEF data. The continuous support of the Van de Graaff crew, D. Roller, E.-P. Knaetsch, and W. Seith, who ran the accelerator in a most efficient way, is gratefully acknowledged. The optimization of the experimental setup would not have been possible without the amazing skill of G. Rupp.

[1] K. Wisshak, F. Voss, F. Käppeler, and G. Reffo, Phys. Rev. C **45**, 2470 (1992).
[2] K. Wisshak, K. Guber, F. Voss, F. Käppeler, and G. Reffo, Phys. Rev. C **48**, 1401 (1993).
[3] F. Voss, K. Wisshak, K. Guber, F. Käppeler, and G. Reffo, Phys. Rev. C **50**, 2582 (1994).
[4] K. Takahashi and K. Yokoi, At. Data Nucl. Data Tables **36**, 375 (1987).
[5] E. Anders and N. Grevesse, Geochim. Cosmochim. Acta **53**, 197 (1989).
[6] H. Beer and R.L. Macklin, Astrophys. J. **331**, 1047 (1988).
[7] N. Prantzos, M. Hashimoto, M. Rayet, and M. Arnould, Astron. Astrophys. **238**, 455 (1990).
[8] W. Howard, B. Meyer, and S. Woosley, Ap. J. **373**, L5 (1991).
[9] C.M. Raiteri, R. Gallino, M. Busso, D. Neuberger, and F. Käppeler, Astrophys. J. **419**, 207 (1993).
[10] D. E. Hollowell and I. Iben, Jr., Astrophys. J. **333**, L25 (1988).
[11] R. Gallino, M. Busso, G. Picchio, and C. Raiteri, Astrophys. J. **334**, L45 (1988).
[12] M. J. Harris, Ap. Space Sci. **77**, 357 (1981).
[13] J. A. Holmes, S. E. Woosley, W. A. Fowler, and B. A. Zimmerman, At. Data Nucl. Data Tables **18**, 305 (1976).
[14] F. Corvi, A. Prevignano, H. Liskien, and P. B. Smith, Nucl. Instrum. Methods A **265**, 475 (1988).
[15] K. Wisshak, F. Voss, F. Käppeler, K. Guber, L. Kazakov, N. Kornilov, M. Uhl, and G. Reffo, Report No. FZKA-5510, Forschungszentrum Karlsruhe, 1995.
[16] K. Wisshak, K. Guber, F. Käppeler, J. Krisch, H. Müller, G. Rupp, and F. Voss, Nucl. Instrum. Methods A **292**, 595 (1990).
[17] K. Wisshak, F. Voss, F. Käppeler, and G. Reffo, Phys. Rev. C **42**, 1731 (1990).
[18] F. H. Fröhner, Technical report, Gulf General Atomic (unpublished).
[19] C. Nordborg, H. Gruppelaar, and M. Salvatores, in *Nuclear*

Data for Science and Technology, edited by S. Qaim (Springer, Berlin, 1992), p. 782.
[20] V. McLane, C. L. Dunford, and P. F. Rose, in *Neutron Cross Sections, Vol. 2* (Academic Press, New York, 1988).
[21] Z. Y. Bao and F. Käppeler, At. Data Nucl. Data Tables **36**, 411 (1987).
[22] G. Reffo, F. Fabbri, K. Wisshak, and F. Käppeler, Nucl. Sci. Eng. **80**, 630 (1982).
[23] M. Uhl and J. Kopecky, in *Nuclei in the Cosmos*, edited by F. Käppeler and K. Wisshak (IOP Publishing, Bristol, 1993), p. 259.
[24] F. Käppeler, K. Wisshak, and K. Guber, Proceedings of a Specialists' Meeting on Measurement, Calculation and Evaluation of Photon Production Data, Bologna, Italy, 1994, p. 247.
[25] N. Weber, diploma thesis, University of Karlsruhe, 1993.
[26] J. F. Mughabghab, M. Divadeenam, and N. E. Holden, *Neutron Cross Sections, Vol. 1, Part A* (Academic Press, New York, 1981).
[27] A. Gilbert and A.G.W. Cameron, Can. J. Phys. **43**, 1446 (1965).
[28] R. L. Macklin (private communication).
[29] W. Ratynski and F. Käppeler, Phys. Rev. C **37**, 595 (1988).
[30] V.S. Shorin, V.N. Kononov, and E.D. Poletaev, Sov. J. Nucl. Phys. **19**, 2 (1974).
[31] R.L. Macklin, Nucl. Sci. Eng. **95**, 304 (1987).
[32] H. Beer, F. Voss, and R.R. Winters, Astrophys. J. Suppl. **80**, 403 (1992).
[33] H. Beer, F. Käppeler, K. Yokoi, and K. Takahashi, Astrophys. J. **278**, 388 (1984).
[34] Y. Nakajima, I. Tsubone, M. Mizumoto, Y. Furuta, M. Ohkubo, M. Sugimoto, and Y. Kawarasaki, Ann. Nucl. Energy **16**, 589 (1989).
[35] V.N. Kononov, B.D. Yurlov, E.D. Poletaev, and V.M. Timokhov, Sov. J. Nucl. Phys. **27**, 5 (1978).
[36] M.V. Bokhovko, A.A. Woewodskij, V.N. Kononov, E.D. Poletaev, and V.M. Timokhov, Report No. FEI-2169, Fiziko Energetscheskij Institut, Obninsk, 1991.
[37] B.V. Thirumala Rao, J. Rama Rao, and E. Kondaiah, J. Phys. A **5**, 468 (1972).
[38] D.C. Stupegia, M. Schmidt, C.R. Keedy, and A.A. Madson, J. Nucl. Energy **22**, 267 (1968).
[39] H. Stoll, Diplomarbeit, University of Karlsruhe, 1993.
[40] K. Toukan, K. Debus, F. Käppeler, and G. Reffo, Phys. Rev. C **51**, (1995).
[41] F. Käppeler, in *Radioactive Nuclear Beams*, edited by T. Delbar (Adam Hilger, Bristol, 1992), p. 305.
[42] S. Jaag and F. Käppeler, Phys. Rev. C **51**, 3465 (1995).
[43] R. Anderl, F. Schmittroth, and Y. Harker, Technical report (unpublished).
[44] M. Rayet, M. Arnould, M. Hashimoto, N. Prantzos, and K. Nomoto, Astron. Astrophys. **298**, 517 (1995).
[45] M. Rayet (private communication).
[46] J. De Laeter (private communication).
[47] F. Käppeler, R. Gallino, M. Busso, G. Picchio, and C. Raiteri, Astrophys. J. **354**, 630 (1990).
[48] E. Burbidge, G. Burbidge, W. Fowler, and F. Hoyle, Rev. Mod. Phys. **29**, 547 (1957).
[49] P. Seeger, W. Fowler, and D. Clayton, Astrophys. J. Suppl. **97**, 121 (1965).
[50] R. Ward, M. Newman, and D. Clayton, Astron. Astrophys. **103**, 189 (1981).
[51] I. Iben, Jr. and A. Renzini, Astrophys. J. **259**, L79 (1982).
[52] I. Iben, Jr. and A. Renzini, Astrophys. J. **263**, L23 (1982).
[53] O. Straniero, R. Gallino, M. Busso, A. Chieffi, C. Raiteri, M. Limongi, and M. Salaris, Astrophys. J. **440**, L85 (1995).
[54] H. Beer, G. Walter, and R. Macklin, in *Capture Gamma-Ray Spectroscopy and Related Topics*, edited by S. Raman (AIP, New York, 1985), p. 778.
[55] S. Jaag, Wissenschaftliche Berichte FZKA-5554 Forschungszentrum Karlsruhe, 1995.
[56] S. Jaag, Diplomarbeit, University of Karlsruhe, 1990.
[57] R. Gallino (private communication).